

A Cross-Hierarchical Multi-Feature Fusion Network Based on Multiscale Encoder–Decoder for Hyperspectral Change Detection

Mingshuai Sheng, BHATTI UZAIR ASLAM, *Senior Member, IEEE*, Junfeng Zhang, *Senior Member, IEEE*, Siling Feng, Yonis Gulzar

Abstract—Hyperspectral change detection (HCD) aims to accurately identify land-cover changes in hyperspectral remote sensing images acquired over the same area at different time points, and holds significant research value in applications such as environmental monitoring and disaster assessment. To address the limitations of existing methods, including insufficient utilization of multiscale features and low efficiency in differential feature fusion, this paper proposes a cross-hierarchical multi-feature fusion network (CHMFFN) based on a multiscale encoder-decoder architecture. First, the front-end of the proposed network adopts a multiscale feature extraction subnetwork, which is built upon an encoder-decoder backbone and enhanced with residual connections and a dual-core channel-spatial attention (DCCSA) module to extract spectral-spatial-temporal features (SSTF). The encoder captures multiscale features ranging from shallow details to deep semantics by leveraging residual blocks and convolutional kernels with varying receptive fields, while the decoder gradually restores spatial resolution and suppresses background noise and redundant information through skip connections that integrate multiscale features from the encoder. Furthermore, a spectral-temporal change feature learning (STCFL) module is proposed to learn change features at different levels between bi-temporal hyperspectral images, thereby strengthening the model's capability to capture inter-temporal differences. An adaptive fusion of advanced features (AFAF) module is also introduced to dynamically balance the contributions of hierarchical differential features by assigning adaptive feature weights, improving the model's representation capability for complex change patterns. Experimental results on four publicly available hyperspectral datasets demonstrate that the proposed CHMFFN outperforms several state-of-the-art methods, verifying its effectiveness.

Index Terms—Hyperspectral change detection, Encoder-Decoder network, multiscale feature fusion, attention mechanism, deep learning.

I. INTRODUCTION

This work was supported in part by Key Research Project of Hainan Province under Grant ZDYF2021SHFZ093, the Natural Science Foundation of China under Grants 62063004 and 62162022, the Hainan Provincial Natural Science Foundation of China under Grants 2019RC018, 5210N206 and 6190N249, the Major Scientific Project of Zhejiang Lab 2020ND8AD01, and the Scientific Research Foundation for Hainan University (No. KYOD(ZR)21013). (Corresponding author: BHATTI UZAIR ASLAM.)

Mingshuai Sheng is currently pursuing a Ph.D. in Information and Communication Engineering at the School of Information and Communication Engineering, Hainan University, Haikou, China (mingshuai@hainanu.edu.cn).

BHATTI UZAIR ASLAM, Junfeng Zhang, and Siling Feng are currently employed at the Department of Artificial Intelligence, School of Information and Communication Engineering, Hainan University, Haikou, China (uzairaslamh@hainanu.edu.cn; jfzhang@hainanu.edu.cn; fengsiling@hainanu.edu.cn).

Yonis Gulzar is employed at the Department of Management Information Systems, King Faisal University, Al-Ahsa, Saudi Arabia (younisgulzar@gmail.com).

HYPERSPECTRAL images (HSI) provide continuous spectral information and integrate spatial and spectral features, enabling simultaneous representation of spatial structures and spectral signatures [1]. These properties make HSI highly effective for detecting changes [2] between multi-temporal images, with applications in land cover classification and disaster assessment [3]. Hyperspectral change detection (HCD) has broad potential [4], [5] in environmental monitoring, disaster loss assessment, and agricultural resource investigation by analyzing data from different time phases to detect changes in land surface types, distribution, and states. This information supports resource management, environmental governance, and disaster response [6]. The core objective of HCD is to identify differences across two temporal instances, with the main challenge being discrimination between changed and unchanged regions [7] in high-dimensional spectral space.

HCD techniques are generally classified into two major categories: traditional methods and deep learning-based approaches [8]. Early studies primarily relied on statistical and algebraic techniques, with representative methods including Spectral Angle Mapping [9] (SAM) and Change Vector Analysis [10] (CVA). These methods detect spectral variations by computing indicators such as the angle and Euclidean distance between spectral vectors. Another group of traditional methods involves feature transformation and dimensionality reduction, such as Principal Component Analysis [11] (PCA), K-means [12] clustering, and Independent Component Analysis [13] (ICA), which aim to extract meaningful change features from complex hyperspectral data. Despite their contributions, traditional approaches suffer from several limitations: they are highly sensitive to predefined parameter settings and exhibit poor robustness to perturbations such as spectral noise and illumination variations, making it difficult to ensure reliable detection performance.

In recent years, deep learning (DL) has achieved remarkable success in various fields, including computer vision and remote sensing. Compared with traditional change detection (CD) models, DL models offer advantages such as automatic feature learning from data, nonlinear modeling of change patterns, strong generalization capability, and efficient fusion of multi-dimensional information. These advantages have established DL as a dominant approach in current hyperspectral change detection research. To improve the performance of HCD algorithms and overcome the limitations of traditional methods, researchers have proposed various DL-based feature extraction and fusion schemes [14]–[17], aiming to enhance detection

accuracy and more precisely characterize the changed regions in hyperspectral images.

Convolutional neural networks (CNNs), as a classic deep learning architecture, achieve efficient joint extraction of local spatial and spectral features from input data within an end-to-end learning framework. Ou et al. [18] proposed a CNN framework combining slow-fast band selection (SFBS) and feature fusion grouping (SFBS-FFGNET), which effectively extracts and separates changed and unchanged features, thereby improving change detection accuracy. Seydi et al. [19] introduced a novel architecture for binary and multi-class hyperspectral change detection based on spectral unmixing and CNN, leveraging pseudo-data generated by the model to train the network for producing multiple change feature maps. Zheng et al. [20] designed a cross-layer CNN architecture based on UNet, which deeply fuses multiscale spatial features with multi-level contextual information through a custom cross-layer block (CLB). Recently, Transformer-based architectures, known for their strength in modeling sequential temporal data, have been integrated into HCD algorithms to better capture temporal dependencies in hyperspectral data. Wang et al. [2] proposed the Spectral-Spatial Temporal Transformer model, which enhances change detection accuracy by extracting and integrating spectral, spatial, and temporal features. Zhang et al. [21] developed a cascaded spectral-aware Transformer architecture aimed at improving temporal relevance and spatial globality extraction, effectively capturing long-term dependencies and spectral-spatial features. Zhang et al. [22] presented a dual-branch siamese spatial-spectral Transformer attention network, designed to comprehensively extract spectral and sequential attribute features via spatial attention and spectral Transformer modules. Lin et al. [23] proposed an unsupervised Transformer-based multivariate detection method, combining compressed change vector analysis and IR-MAD for pseudo-training sample generation. This method utilizes IR-MAD for subtle change detection and employs the Transformer attention mechanism to model pixel-wise differences and similarities, yielding more accurate and robust detection results.

The attention mechanism is a computational strategy inspired by the way human attention allocates focus. As a key component in deep learning [24], its core idea is that information processing selectively emphasizes important features while suppressing less relevant ones, thereby enhancing the model's capability to capture critical information and improving processing efficiency. This dynamic weighting scheme effectively addresses the issue of feature redundancy caused by the fixed receptive fields [25] in traditional convolutional networks. In hyperspectral change detection, various attention-based detection frameworks have been developed to improve accuracy. For instance, Gong et al. [26] proposed a novel Spectral-Spatial Attention Network (S2AN) that employs adaptive spectral and spatial attention mechanisms to suppress irrelevant information for change detection. Hu et al. [27] introduced the Global Multi-head Interactive Self-attention Change Detection Network (GlobalMind), designed to capture correlations among surface objects and land cover transformations, facilitating more comprehensive data analysis and accurate detection. Jiang et al. [17] presented the Adaptive

Center-Focused Hybrid Attention Network (ACFHAN), which adaptively enhances spatial regions and spectral channels most pertinent to change while suppressing noise. Ren et al. [28] developed the Interactive Supervised Dual-mode Attention Network (ISDANet). In the encoding stage, ISDANet utilizes MobileNetV2 to extract bi-temporal features, aggregates multiscale semantic features via NFAM to enhance temporal representation, and integrates self-attention with cross-attention through IAEM to enable deep interaction between bi-temporal features. During decoding, it re-weights differential features using SAM and incorporates supervisory signals to dynamically fuse multiscale features, thereby improving boundary detection accuracy and sensitivity to subtle changes.

Previous studies have identified two core optimization directions in HCD: efficient feature extraction and the design of multi-stage feature fusion mechanisms. First, it is critical to address the trade-off between network depth and feature representation capacity—shallow architectures often fail to extract representative features, whereas overly deep or complex networks may result in both computational and feature redundancy, potentially leading the model to learn noisy or irrelevant features. Second, most existing deep learning-based HCD methods utilize RNN or LSTM architectures for bi-temporal feature fusion. However, these approaches lack a decoupling mechanism between changed and unchanged components, forcing the model to concurrently learn dynamic changes and static background information, which increases the difficulty of detecting subtle changes. Additionally, conventional fusion strategies do not incorporate adaptive weighting based on feature relevance, thereby limiting their ability to highlight dominant change features and accurately capture fine-grained differences. Notably, multiscale feature representations have shown considerable promise in improving micro-change detection [29], [30]. Therefore, this study proposes a multiscale learning framework that enhances HCD performance by decoupling changed-unchanged components, employing dynamic feature weighting strategies, and integrating multiscale spatial-spectral information.

In summary, this paper proposes a Cross-Hierarchical Multi-Feature Fusion Network based on a multiscale encoder-decoder architecture. The proposed CHMFFN consists of four key modules: (1) the Dual-Core Channel-Spatial Attention Module (DCCSA), (2) the Multiscale Encoder-Decoder Module (MSED), (3) the Spectral-Temporal Change Feature Learning Module (STCFL), and (4) the Advanced Feature Adaptive Fusion Module (AFAF). Among these, the DCCSA and MSED jointly form the spectral-temporal multiscale feature extraction subnetwork. Specifically, DCCSA is designed to identify salient feature channels and emphasize informative spatial regions, while MSED captures hierarchical multiscale representations from hyperspectral data. Subsequently, STCFL is employed to jointly model spectral, spatial, and temporal dependencies, and AFAF adaptively fuses the extracted features to generate discriminative and change-sensitive representations. The main contributions of this work are summarized as follows:

- 1) A DCCSA Module is proposed to dynamically assign attention weights across spectral channels and spatial

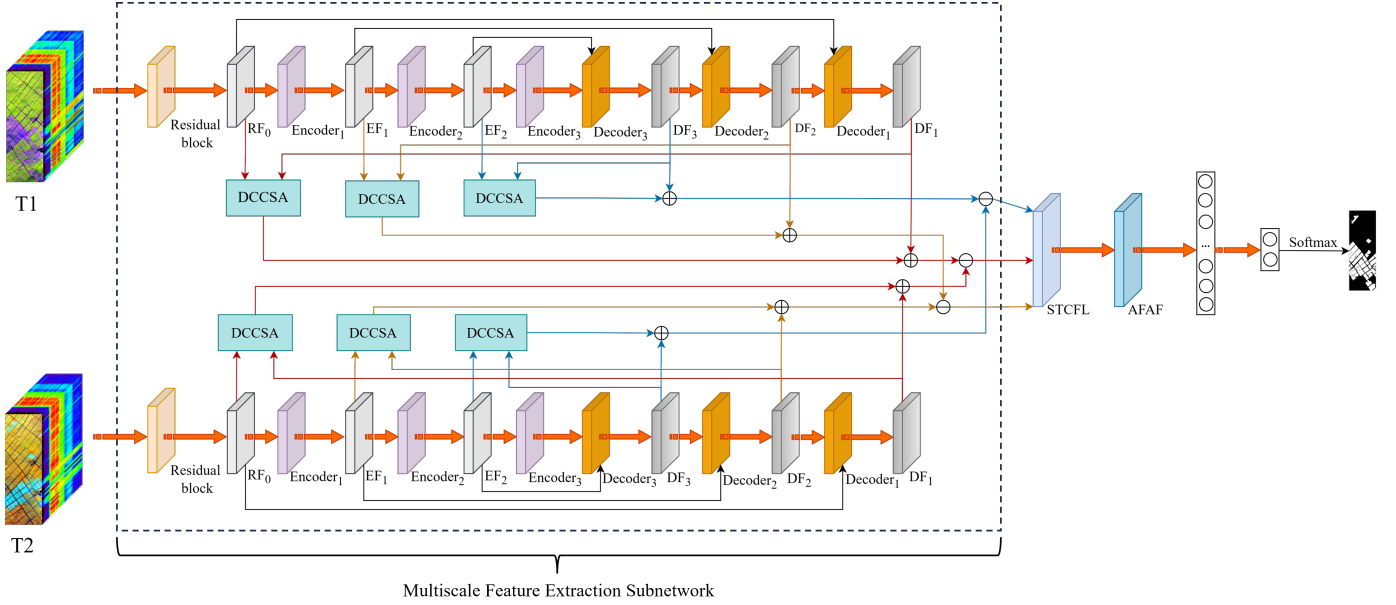


Fig. 1. Overall structure diagram of CHMFFN.

regions. This module emphasizes task-relevant features through a hierarchical attention mechanism, thereby enhancing the model's ability to focus on salient information and improving the accuracy of feature representation.

- 2) A spectral-temporal multiscale feature extraction subnetwork is designed to extract discriminative spectral-temporal features from bi-temporal HSI. An encoder-decoder architecture is employed as the backbone, where multiscale convolutional modules are integrated to expand the receptive field. Furthermore, residual connections and skip connections embedded with channel-spatial attention (CSA) modules are introduced to effectively fuse contextual information and enhance feature representation.
- 3) The proposed spectral-temporal (ST) change feature learning module aims to effectively learn and integrate bi-temporal differential representations. Specifically, by leveraging cross-temporal fusion and deep feature interaction, this module further enhances the model's ability to capture subtle changes in HSI.
- 4) An AFAP Module is proposed to perform the final integration of key change features extracted from preceding modules. This module is designed to exploit complementary information from multiple feature maps and generate highly discriminative spatial-spectral-temporal representations for accurate change detection.

The remainder of this paper is organized as follows. Section II presents the details of the proposed CHMFFN architecture. Section III describes the four experimental datasets, parameter settings, and experimental results, including ablation and comparative studies. Finally, Section IV concludes the paper and outlines directions for future research.

II. PROPOSED METHOD

This section elaborates on the architecture of the proposed Cross-Hierarchical Multi-Feature Fusion Network, as illustrated in Fig. 1. The framework primarily consists of three components: a multiscale feature extraction subnetwork, a spectral-temporal (ST) change feature learning module, and an advanced feature adaptive fusion module. The model progressively extracts multiscale spectral-temporal features from the input bi-temporal HSI. Subsequently, the STCFL module performs initial feature fusion and representation learning. Thereafter, the adaptive fusion module further refines and integrates these features, which are finally fed into an MLP classifier to perform change detection. The detailed design of each module will be introduced in the following subsections.

A. Multiscale feature extraction subnetwork

1) *Structure of the multiscale feature extraction subnetwork:* Due to their strong capabilities in data modeling and feature learning, CNNs are widely employed in HCD tasks to extract spatial-spectral [31] joint features. However, most existing methods integrate feature from only a single level, either at the input or output stage, which often results in the loss of critical information. Low-level features typically capture fine spatial details, such as textures and edges [32], [33], while high-level features tend to encode abstract and coarse semantic information. This imbalance makes it difficult to generate accurate and well-defined boundaries. Therefore, the fusion of multiscale and multi-level information is essential for more precise representation of HSI feature.

In light of the above considerations, we propose a multiscale feature extraction subnetwork (MSFES) module. The structure of the module is illustrated in Fig. 2, where RF, EF, and DF denote the output features from the residual block, encoder, and decoder layers, respectively. This subnetwork aims to ex-

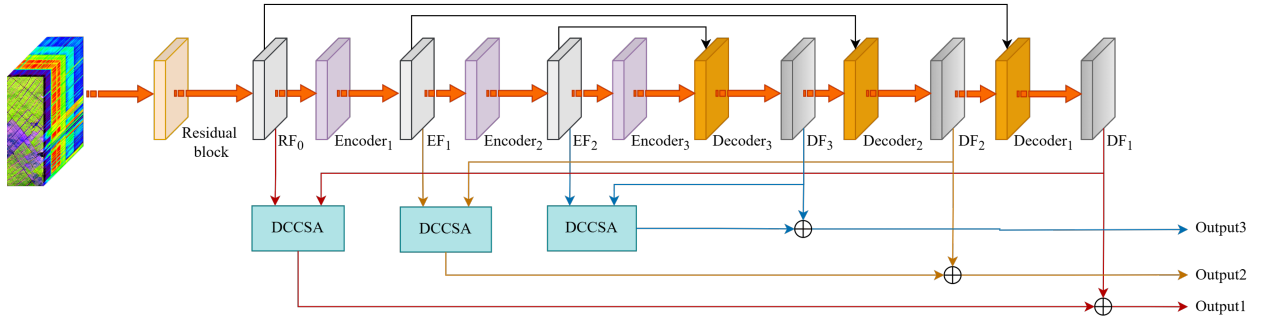


Fig. 2. Structure of the multiscale feature extraction subnetwork.

tract and integrate multiscale hierarchical features from residual blocks, multiscale encoders, and decoders to enrich the spectral-spatial-temporal representations of hyperspectral data. The residual block performs initial preprocessing and encodes the spatial-spectral characteristics of the input. Subsequently, the multiscale encoder, consisting of convolutional layers with various kernel sizes, further encodes the extracted information to comprehensively capture spectral-spatial-temporal features. The decoder then generates refined feature representations based on the joint features from the encoder. To improve the decoder's ability to reconstruct detailed target information, a DCCSA module is embedded within the MSFES. This attention variant aims to extract and convey highly relevant joint feature information between low-level and high-level layers. Unlike conventional attention mechanisms, DCCSA incorporates enhanced dual-core channel attention and spatial attention components, offering more discriminative and informative attention weights.

2) *Residual block*: As illustrated in Fig. 3, the residual block consists of two consecutive 3×3 convolutional layers, each followed by batch normalization (BN) and the self-regularizing Mish activation function. A skip connection is incorporated in parallel, which adjusts the feature dimensions via a 1×1 convolution followed by BN. This design improves the diversity of feature extraction and enhances the training stability of the network. Given the input patch h_I , the final output of the residual block, denoted as Out_r , can be mathematically formulated as:

$$Out_r = \sigma_{Mish}(BN_2(Conv_2(\sigma_{Mish}(BN_1(Conv_1(h_I)))))) + BN(Conv(h_I)) \quad (1)$$

where $\sigma_{Mish}(\cdot)$ denotes the Mish activation function, whose definition is as follows:

$$Mish(x) = x \cdot \tanh(\ln(1 + e^x)) \quad (2)$$

3) *Encoder module*: Each encoder consists of three parallel convolutional layers followed by a standard Transformer encoder. The convolution kernel sizes are 3×3 , 5×5 , and 7×7 , respectively. Each convolutional layer is followed by a batch normalization layer. The structure of the encoder is depicted in Fig. 4, which illustrates from left to right the overall architecture of the multiscale encoder, the multi-head attention mechanism, and the scaled dot-product attention structure.

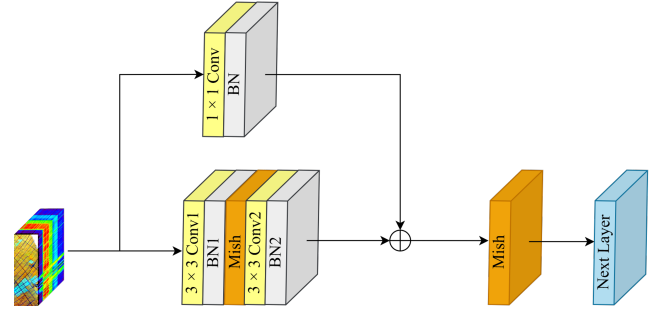


Fig. 3. Structure of the residual block.

The output feature map of the encoder can be mathematically described as:

$$E_{output} = LN(LN(x_{pos} + MHSA(x_{pos})) + FFN(LN(x_{pos} + MHSA(x_{pos})))) \quad (3)$$

Here, x_{pos} denotes the input feature that incorporates positional encoding information. $MSHA$ stands for multi-head self-attention, FFN denotes the feed-forward network, and LN represents the layer normalization. The calculation process of x_{pos} is as follows:

$$x_{pos} = Concat(\sigma_{Mish}(BN(Conv_{3 \times 3}(x))), \sigma_{Mish}(BN(Conv_{5 \times 5}(x))), \sigma_{Mish}(BN(Conv_{7 \times 7}(x)))) + PE(\cdot) \quad (4)$$

where $PE(\cdot)$ denotes the encoding of input features, and $Concat(\cdot)$ represents the concatenation of feature.

4) *Decoder module*: As illustrated in Fig. 5, each decoder layer comprises a Masked Multi-Head Self-Attention mechanism, a Multi-Head Cross-Attention mechanism, a Feed-Forward Network (FFN), as well as residual connections and layer normalization applied via the “Add & Norm” operation. Before entering the decoder, input features are first processed by positional encoding and output embedding. Each component promotes effective gradient propagation through residual paths and stabilizes training through normalization. The output

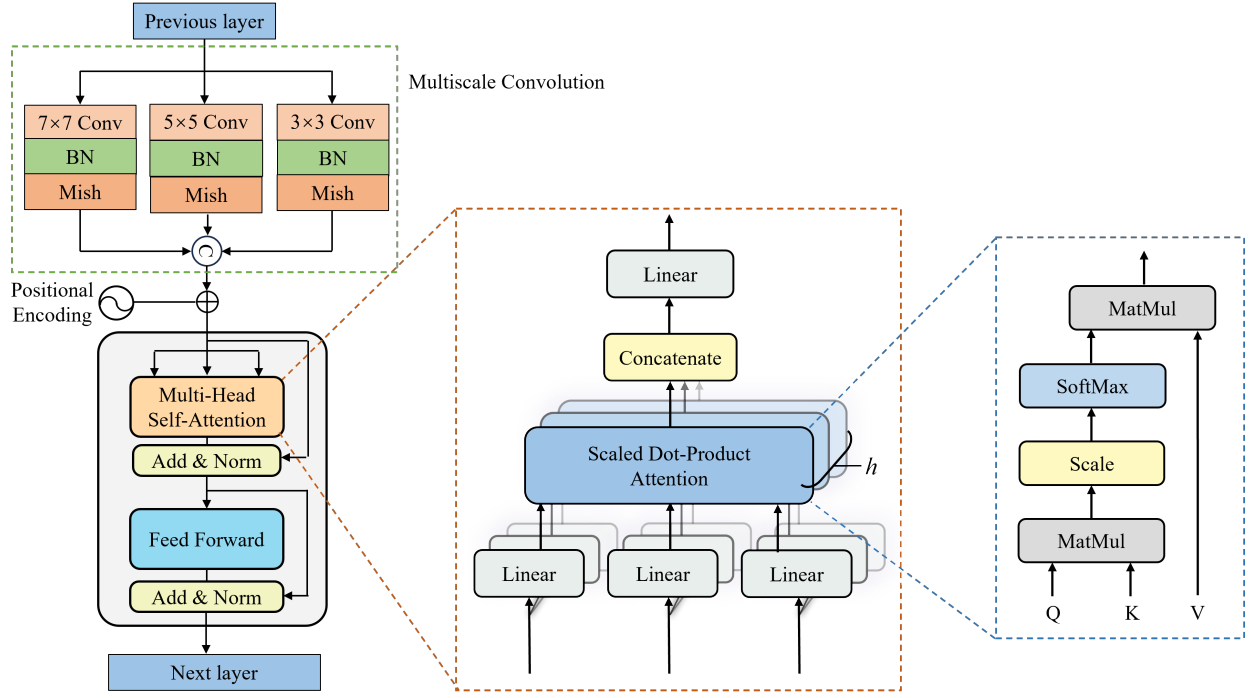


Fig. 4. Structure diagram of the encoder. From left to right: multiscale encoder, multi-head self-attention, and scaled dot-product attention.

of the decoder, denoted as D_{Output} , is given by:

$$D_{Output} = LN(x_{cross-attn} + FFN(x_{cross-attn})) \quad (5)$$

$$x_{cross-attn} = LN(x_{masked-attn} + MHSA(x_{cross-attn}, E_{Output}, E_{Output})) \quad (6)$$

$$x_{masked-attn} = LN(x_{embed+pe} + MHSA_{masked}(x_{embed+pe})) \quad (7)$$

$$x_{embed+pe} = Embed(x_{shifted}) + PE(x_{shifted}) \quad (8)$$

where $x_{cross-attn}$ is the output value of the second “Add & Norm” layer of the decoder associated with the encoder, $x_{masked-attn}$ is the output value of the first “Add & Norm” layer, $Embed(\cdot)$ denotes the embedding operation, E_{Output} is the encoder output, and $x_{embed+pe}$ is the input value of the decoder.

5) *Dual-core channel-spatial attention module*: To enhance attention weights for better highlighting of important features, we introduce two parallel convolutional layers into both the channel and spatial attention branches, forming a novel dual-core attention module. The module employs a cascaded design combining enhanced channel and spatial attention mechanisms, enabling joint processing of input features. Its structure is shown in Fig. 6. The input feature tensor F first passes through the channel attention branch, where it undergoes parallel 3×3 and 5×5 convolutions to extract and fuse multiscale features, followed by a shared MLP layer for learning discriminative representations. Finally, the MLP outputs are combined via element-wise addition and passed through a Sigmoid activation function to generate the attention weight W . The input F is then multiplied by W to obtain the channel attention output $Output_c$.

$$Output_c = F_1 \cdot \sigma_{Sigmoid}(W) \quad (9)$$

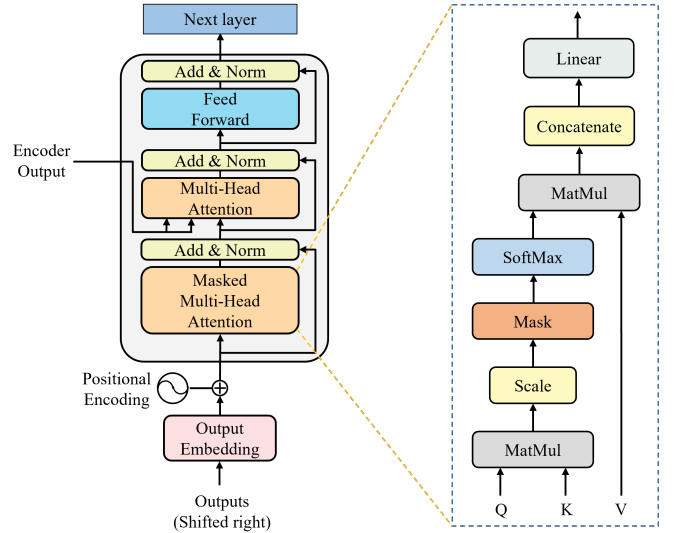


Fig. 5. Structure of the decoder.

Where F is the input feature, W is the attention weight matrix, and $\sigma_{Sigmoid}(\cdot)$ denotes the activation operation performed using the Sigmoid activation function.

$$W = Conv_{1 \times 1}(\sigma_{Mish}(Conv_{1 \times 1}(MaxPool(F_{conv})))) + Conv_{1 \times 1}(\sigma_{Mish}(Conv_{1 \times 1}(AvgPool(F_{conv})))) \quad (10)$$

$$F_{conv} = Conv_{3 \times 3}(F) + Conv_{5 \times 5}(F) \quad (11)$$

The spatial attention module takes the channel-refined feature F_c as input. To aggregate spatial information, both max pooling and average pooling operations are applied, and their outputs are concatenated to form a multiscale feature

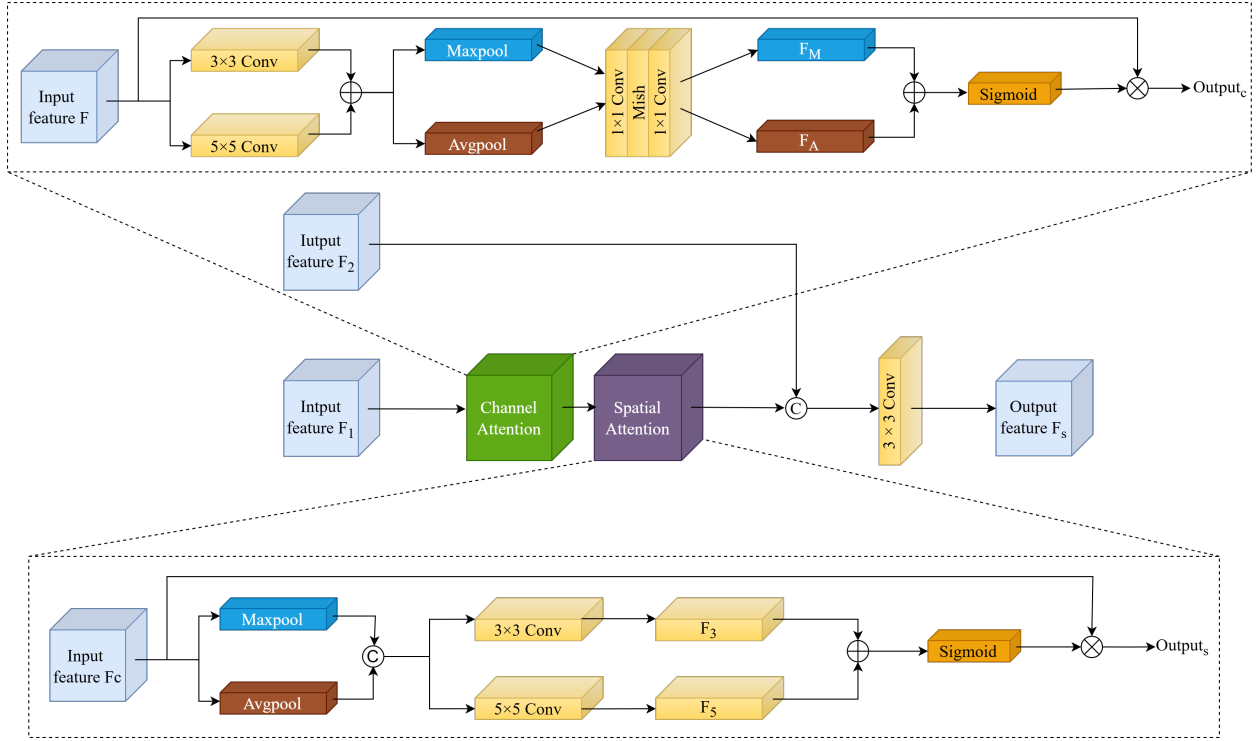


Fig. 6. Structure of the DCCSA.

representation. These concatenated features are then processed by 3×3 and 5×5 convolutional layers, respectively, to capture details from different receptive fields. After feature fusion, spatial attention weights are generated via the Sigmoid activation function and used to weight F_c , resulting in the spatial attention output F_s . By leveraging a decoupled structure of channel and spatial attention mechanisms, this module enables adaptive enhancement of both channel-wise and spatial feature representations, thereby improving the model's ability to capture critical information. The output is computed as follows:

$$F_s = \text{Conv}_{3 \times 3}(\text{Concat}(F_2, F_c \cdot \sigma_{\text{Sigmoid}}(\text{Conv}_{3 \times 3}(F_{\text{pool}}) + \text{Conv}_{5 \times 5}(F_{\text{pool}})))) \quad (12)$$

$$F_{\text{pool}} = \text{Concat}(\text{MaxPool}(F_c), \text{AvgPool}(F_c)) \quad (13)$$

Where F_c is the output value Output_c of the channel attention module, $\text{Concat}(\cdot)$ represents the concatenation operation, and $\sigma_{\text{Sigmoid}}(\cdot)$ denotes the activation operation of the activation function.

B. Spectral-Temporal Change Feature Learning Module

In bi-temporal HSI processing, the input image patches are first passed through a multiscale feature extraction subnetwork, resulting in three feature maps with varying levels and multiple scales. These feature maps consist of both change and invariant components. Among them, the change components possess stronger representational capacity for fine-grained changes and directly contribute to the core objective of change pixel detection. However, existing studies often overlook the targeted learning of change components within spectral-spatial-temporal joint features during change detection. To address

this issue, this paper proposes a Spectral-Temporal Change Feature Learning (STCFL) module, which effectively captures subtle change features through a multi-dimensional feature interaction mechanism. The detailed architecture of the proposed module is illustrated in Fig. 7.

The module adopts a multi-branch parallel architecture that integrates 1×1 convolutions, multi-stage 3×3 convolutions, and a dense residual connection mechanism to construct a spectral-spatial-temporal joint feature learning framework. Specifically, each branch generates multi-granularity representations by extracting features at different scales. Then, deeper features are obtained through stage-wise convolutions, and feature maps from different levels are fused using cross-layer residual connections. The three output expressions of the module are defined as follows:

$$\text{Output}_1 = (\text{BN}(\text{Conv}_{1 \times 1}(F_1)) + \sigma_{\text{ReLU}}(\text{BN}(\text{Conv}_{3 \times 3}(X_2)))) + \text{Concat}(X_1, X_2) \quad (14)$$

$$\text{Output}_2 = \text{Concat}(X_1, X_2) \quad (15)$$

$$\text{Output}_3 = \sigma_{\text{ReLU}}(\text{BN}(\text{Conv}_{3 \times 3}(X_1))) + \text{BN}(\text{Conv}_{1 \times 1}(F_3)) + \text{Concat}(X_1, X_2) \quad (16)$$

$$X_1 = \text{BN}(\text{Conv}_{1 \times 1}(F_1)) + \text{BN}(\text{Conv}_{1 \times 1}(F_2)) \quad (17)$$

$$X_2 = \text{BN}(\text{Conv}_{1 \times 1}(F_2)) + \text{BN}(\text{Conv}_{1 \times 1}(F_3)) \quad (18)$$

where F_1 , F_2 , and F_3 denote the three inputs of the module (feature output value of the feature extraction subnetwork), $\text{BN}(\cdot)$ stands for the batch normalization operation.

This design strategy offers three advantages: First, the multi-branch parallel structure effectively captures initial features

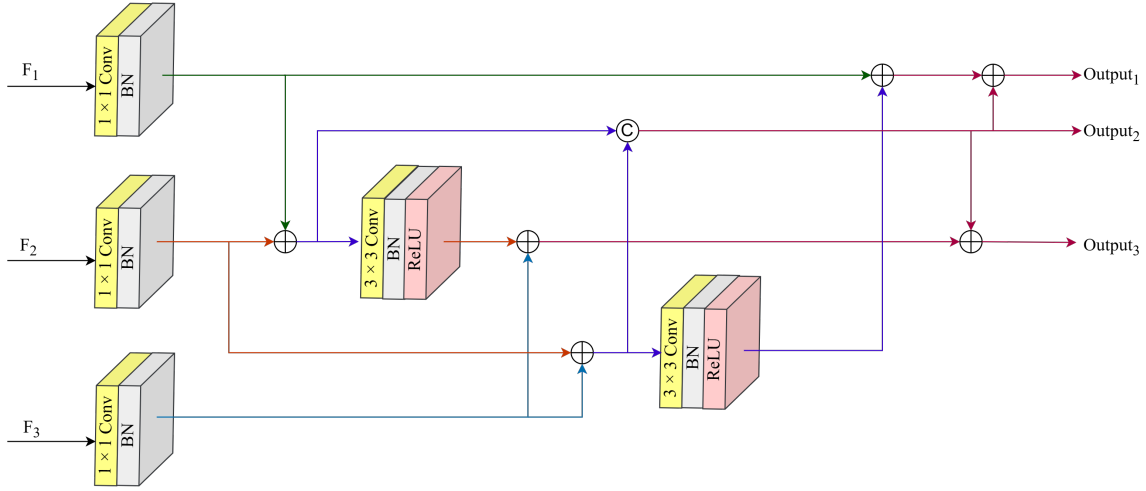


Fig. 7. Structure of the STCFL module.

at different scales, enhancing information diversity through multi-path feature extraction. Second, the dense residual connection mechanism constructs shortcut paths for gradient propagation, significantly alleviating the gradient vanishing problem in deep networks and supporting the training of deeper models. Third, the cross-layer feature fusion strategy realizes complementary reuse of features at different levels, preserving shallow detail information while fusing deep semantic features, thereby enhancing the robustness of feature expression and improving the model's ability to model complex change patterns.

C. Advanced Feature Adaptive Fusion Module

After being processed by the STCFL module, three feature maps containing information at different spatial scales are generated. In traditional approaches, these multiscale features are typically fed directly into a fully connected layer for fusion, with final change detection performed using activation functions such as Sigmoid or SoftMax. However, this straightforward integration often results in suboptimal detection performance due to insufficient emphasis on salient information. As previously discussed, attention mechanisms help focus on important features and have been increasingly applied [34] in the field of HCD. For example, Shangguan Y et al. [35] proposed an ACSP attention structure to explore the multiscale contextual information of coarse change features. ACSP employs contextual self-attention (CSA) branches with varying dilation rates to extract multiscale semantics, thereby improving the model's ability to adaptively perceive and capture relevant changes. To address these limitations, this study introduces an adaptive feature aggregation mechanism that complements features across different scales and reinforces key information through dynamic weight allocation. The architectural diagram is shown in Fig. 8.

The AFAM module achieves adaptive fusion of multiscale features by incorporating an attention mechanism. First, 3×3 convolutions are applied to the input features F_{s1} and F_{s3} to enhance local feature representation. Then, the convolution output of F_{s1} and the original F_{s2} features are compressed

into channel-level statistics using Global Average Pooling (GAP). These statistics are subsequently passed through two sequential 1×1 convolution layers (with Batch Normalization and ReLU activation in between) for dimensionality reduction and transformation. After that, normalized attention weights are generated via the Sigmoid function. Each weight is applied to the corresponding feature— F_{s1} , F_{s2} , and F_{s3} —via channel-wise multiplication, enabling dynamic enhancement of important features. Finally, the three weighted features are concatenated along the channel dimension to produce the fused feature map. By adaptively adjusting the contribution of each input, this module improves the effectiveness of multiscale feature fusion and enhances overall feature representation.

$$Output = Concat((Conv_{3 \times 3}(F_{s1}) \times W), (F_{s2} \times W), (Conv_{3 \times 3}(F_{s3}) \times W)) \quad (19)$$

$$W = \sigma_{Sigmoid}(Conv_{1 \times 1}(\sigma_{ReLU}(BN(Conv_{1 \times 1}(GAP(F)))))) \quad (20)$$

$$F = Conv_{3 \times 3}(F_{s1}) + F_{s2} + Conv_{3 \times 3}(F_{s3}) \quad (21)$$

where W is the attention weight matrix, F_{s1}, F_{s2}, F_{s3} are the output values of the STCFL module respectively, and F is the fused feature.

After multi-stage feature extraction by the preceding module, a feature map capturing multiscale change information is generated. This feature map is then passed through a fully connected layer to produce a probability distribution vector, which is subsequently processed by a classifier to obtain the final category label of the input data block, thereby achieving accurate change detection. The final result of HCD can be expressed as follows:

$$y_n = \sigma_{softmax}(F_c(F_c(Conv_{5 \times 5}(Output)))) \quad (22)$$

where y_n is the probability that the input sample is predicted to belong to class n , F_c denotes the fully connected layer, and $Output$ is the output of the AFAM module.

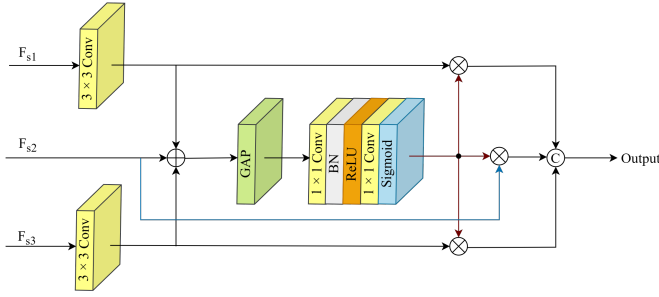


Fig. 8. Structure of the AFAM module.

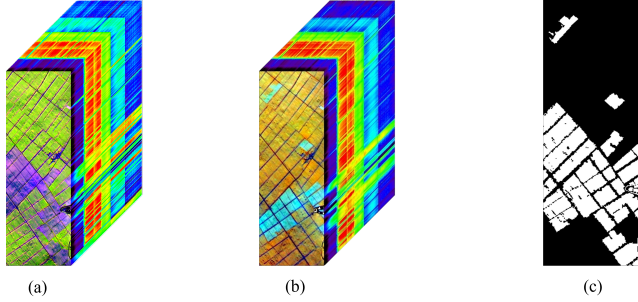


Fig. 9. Farmland dataset. (a) Image acquired on May 3, 2006. (b) Image acquired on April 23, 2007. (c) Change ground truth.

D. Loss Function

In the training of DL model, adopting an appropriate loss function is essential for optimizing the network architecture and guiding the feature extraction module to learn more discriminative representations. In CD tasks, the cross-entropy loss function measures the divergence between the predicted results and ground-truth labels, offering a clear gradient direction for parameter updates. In binary classification scenarios, its optimization is equivalent to maximizing the log-likelihood of the correct class. This property gives it better convergence performance than traditional loss functions such as mean squared error, particularly in pixel-wise classification tasks. Moreover, combining cross-entropy loss with the softmax activation function enables the model to produce outputs that align with probability distributions. This facilitates subsequent threshold segmentation or fine-grained classification, ultimately enhancing the accuracy and spatial coherence of the change detection results. It can be formally expressed as:

$$Loss = -\frac{1}{N} \sum_{i=1}^N (y_i \log(y_n) + (1 - y_i) \log(1 - y_n)) \quad (23)$$

where N is the number of batch samples, y_i is the true label pixel value, and y_n is the predicted probability value belonging to class n .

III. EXPERIMENT

This section begins by briefly introducing the hyperspectral image change detection dataset and the evaluation metrics employed for quantitatively assessing the performance of the proposed CHMFFN method. Subsequently, the experimental results of the proposed algorithm are discussed in detail. The

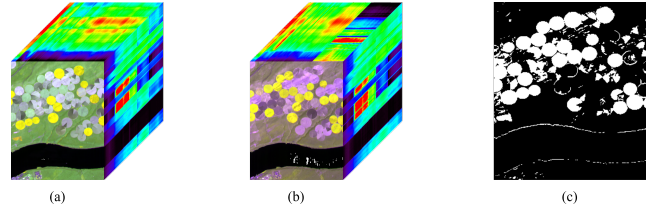


Fig. 10. Hermiston2 dataset. (a) Image acquired on May 1, 2004. (b) Image acquired on May 8, 2007. (c) Change ground truth.

effectiveness of key components, including the multiscale feature extraction module and the adaptive feature fusion module, is verified through modular ablation experiments. In addition, several state-of-the-art HCD algorithms are selected for performance comparison and analysis, with the corresponding experimental hyperparameter settings also provided. Finally, the impacts of training sample proportion, batch size, and input image patch size on network performance are analyzed through controlled experiments.

A. Datasets and Evaluation Metrics

1) *Datasets*: The first dataset is the Yancheng dataset from Jiangsu Province, collected by the Hyperion sensor, hereafter referred to as “Farmland”. As shown in Fig. 9(a) and 9(b), two hyperspectral images, named T1 and T2, were acquired on May 3, 2006, and April 23, 2007, respectively. Each image has dimensions of $420 \times 140 \times 154$, covering 154 spectral bands. Fig. 9(c) presents the manually annotated ground truth of farmland changes, consisting of 40,417 unchanged pixels (black areas) and 18,383 changed pixels (white areas), reflecting the agricultural land transformations near Yancheng City, Jiangsu Province, China.

The second dataset, referred to as “Hermiston2”, was collected by the Hyperion sensor in irrigated farmlands located in Hermiston, Umatilla County, Oregon, USA. As shown in Fig. 10(a) and 10(b), the dataset has a spatial resolution of 307×241 pixels and comprises 154 spectral bands. T1 and T2 were acquired on May 1, 2004, and May 8, 2007, respectively. Fig. 10(c) shows the ground truth of farmland changes, comprising 16,676 changed pixels (white areas) and 57,311 unchanged pixels (black areas), indicating the variations in irrigated farmlands over time in the Hermiston area.

The third dataset, referred to as “Hermiston”, focuses on circular farmlands. It covers agricultural areas in Hermiston, Umatilla County, Oregon, USA, with data collected by the Hyperion sensor on May 1, 2004, and May 8, 2007. As shown in Fig. 11(a) and 11(b), the dataset comprises 242 spectral bands with spatial dimensions of 390×200 pixels. Fig. 11(c) presents the ground truth labels, indicating 9,986 changed pixels (white) and 68,014 unchanged pixels (black), which reflect actual changes in the circular farmland area.

The fourth dataset, referred to as “River”, represents a riverine region in Jiangsu Province, China. It comprises hyperspectral images acquired by the Hyperion sensor on May 3 and December 31, 2013. As illustrated in Fig. 12(a) and 12(b), this dataset includes 198 spectral bands with a spatial

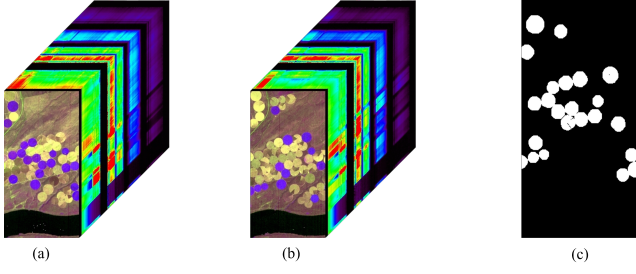


Fig. 11. Hermiston dataset. (a) Image acquired on May 1, 2004. (b) Image acquired on May 8, 2007. (c) Change ground truth.

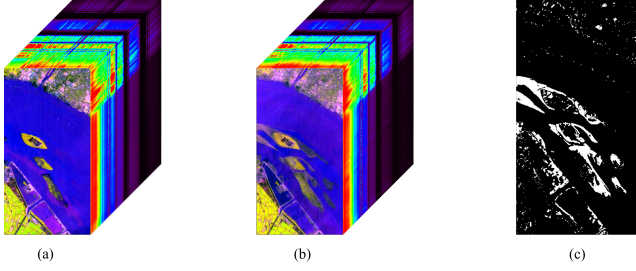


Fig. 12. River dataset. (a) Image acquired on May 3, 2013. (b) Image acquired on December 31, 2013. (c) Change ground truth.

resolution of 463×241 pixels. Fig. 12(c) presents the ground truth map of changes within the river area, comprising 101,885 unchanged pixels (black) and 9,698 changed pixels (white). The primary types of land cover change in this dataset involve variations in river sediment levels and channel morphology.

2) *Evaluation Metrics*: To effectively assess the performance of the proposed method, we compare the predicted detection results with the ground-truth reference data. In this study, Overall Accuracy (OA) and the Kappa Coefficient (KC) are adopted as the primary evaluation metrics, while Precision (Pr), Recall (Re), and F1-score (F1) are employed as supplementary metrics. These metrics [36]–[39] jointly provide a comprehensive evaluation of the proposed algorithm.

OA represents the proportion of correctly predicted samples by the classification model to the total number of samples, reflecting the overall classification accuracy of the model. A larger value indicates a better overall classification effect.

$$OA = \frac{TP + TN}{TP + FP + TN + FN} \quad (24)$$

KC is used to measure the consistency between the prediction results of a classification model and the true results, taking into account the impact of chance factors in the classification results. Compared with Overall Accuracy, it can evaluate model performance more accurately. A larger value indicates a stronger consistency between the model's classification results and the true labels, and this consistency excludes the interference of random factors.

$$KC = \frac{OA - p_e}{1 - p_e} \quad (25)$$

Where the calculation process of the expected accuracy p_e is

as follows:

$$p_e = \frac{(TP \times FN) + (TP \times FP) + (TN \times FN) + (TN \times FP)}{N^2} \quad (26)$$

Pr refers to the proportion of true positive samples among those predicted as positive by the model, measuring the accuracy of the model in predicting positive classes. A larger value indicates a higher proportion of truly positive samples among those predicted as “positive” by the model, i.e., “fewer false positives”.

$$Pr = \frac{TP}{TP + FP} \quad (27)$$

Re, also known as sensitivity or true positive rate, refers to the proportion of samples correctly predicted as positive among all actually positive samples, reflecting the model's ability to identify positive samples. A larger value indicates a higher proportion of truly “positive” samples that are successfully identified by the model, i.e., “fewer false negatives”.

$$Re = \frac{TP}{TP + FN} \quad (28)$$

The F1 is the harmonic mean of precision and recall. It comprehensively considers the model's precision and recall, enabling a more holistic evaluation of model performance. A higher F1-score indicates a better balance between the model's Pr and Re, as well as a superior overall performance of the two.

$$F1 = \frac{2PR}{P + R} \quad (29)$$

Among them, True Positives (TP) refer to the number of samples that are actually positive and correctly predicted as positive by the model. True Negatives (TN) represent the number of samples that are actually negative and correctly predicted as negative. False Positives (FP) denote the number of samples that are actually negative but incorrectly predicted as positive by the model (commonly referred to as false alarms), whereas False Negatives (FN) indicate the number of samples that are actually positive but misclassified as negative (also known as missed detections). In the visualization of the experimental results, TP, TN, FP, and FN pixels are displayed in white, black, green, and red, respectively, to intuitively highlight the model's classification behavior. The final evaluation of the model's performance relies on metrics such as OA, KC, Pr, Re, and F1, which are derived from the above statistical quantities. Higher values of these metrics generally indicate better CD performance.

B. Experimental Hyperparameter Settings

1) *Proposed Model Parameter Settings*: The proposed CHMFFN model is implemented using the PyTorch deep learning framework, and training and testing are conducted on an NVIDIA GTX A100 GPU. During the training phase, the Stochastic Gradient Descent (SGD) optimizer is employed with an initial learning rate of $5e-3$, and the model is trained for a total of 100 epochs. The input image patch size is set to 9×9 , and the batch size is 32. For training and testing partitioning, 30% of the pixels are randomly selected from both changed and unchanged regions to form the training set, while

the remaining pixels are used for testing. The experimental settings are kept consistent across all four datasets.

2) *Comparison Model Parameter Settings*: According to the original papers, for MHCD [40], we selected an input patch size of 9×9 , a batch size of 64, a training set ratio of 5%, 300 training epochs, and an initial learning rate of $1e-4$. For MsFNet [41], the input image patch size was 9×9 , and the Adam optimizer was used during training. The initial learning rate was set to $5e-4$, the batch size to 32, and the number of training epochs to 200. The Diefen [42] algorithm used an input image patch size of 5×5 , an initial learning rate of 0.001, and was trained with an SGD optimizer with a decay weight of $5e-3$. The training set ratio was 1%, the batch size was 64, and the total number of epochs was 100. For AIWSEN [43], the input image patch size was 7×7 , the initial learning rate was $5e-3$, and it was trained using an SGD optimizer with a decay weight of $5e-3$, with a decay factor of 0.1 every 35 epochs. The training set ratio was 1%, the batch size was 64, and the total number of epochs was 100. For MSDFFN [44], the input image patch size was 9×9 , the initial learning rate was $5e-3$, and it was trained using an SGD optimizer with a decay weight of $5e-3$, with a decay factor of 0.1 every 35 epochs. The training set ratio was 20%, the batch size was 32, and the total number of epochs was 100. The DA-Former [45] detection architecture used an input image patch size of 9×9 , an initial learning rate of $5e-4$, and was trained using the Adam optimizer. The training set ratio was uniformly set to 1%, the batch size was 64, and the total number of epochs was 600.

C. Experimental results

1) *Experimental Results on the Farmland Dataset*: Table I presents the results of each model on the Farmland dataset. Compared with the AIWSEN and DA-former methods, other methods perform better in all metrics, with significant improvements in OA and KC. This indicates that the overall performance of the AIWSEN and DA-former algorithms is relatively weak, and their ability to identify changed regions is insufficient, leading to unsatisfactory classification results. Compared with AIWSEN, DA-former, and Diefen, MHCD, MsFNet, MSDFFN, and the proposed method generally exhibit better performance. This is because these methods can more effectively capture the change features of farmland scenes, thereby improving the accuracy of change detection. After introducing better feature extraction and fusion mechanisms, MSDFFN and the proposed method outperform other methods with relatively average performance. This suggests that efficient mechanisms help the network learn more accurate farmland change features to adapt to different land cover change scenarios. Compared with MSDFFN, the proposed method achieves further improvements in all metrics due to its better balance between precision and recall. Therefore, CHMFFN has better comprehensive performance in the change detection task on the farmland dataset.

To present the experimental results more intuitively, we visualized the data in Table I as shown in Fig. 13. Overall, the result images of Diefen, AIWSEN, and DA-former contain

TABLE I
COMPARISON BETWEEN CHMFFN AND VARIOUS METHODS ON THE FARMLAND DATASET

Method	OA (%)	KC (%)	F1 (%)	Pr (%)	Re (%)
MHCD	96.52	91.90	94.44	94.32	94.55
MsFNet	97.26	93.66	95.66	94.67	96.68
DIEFEN	93.47	85.32	90.19	85.04	96.00
AIWSEN	90.13	77.72	85.06	80.71	89.90
MSDFFN	98.08	95.55	96.95	96.13	97.79
DA-former	90.19	78.14	85.49	79.48	92.48
Ours	98.61	96.77	97.78	97.53	98.04

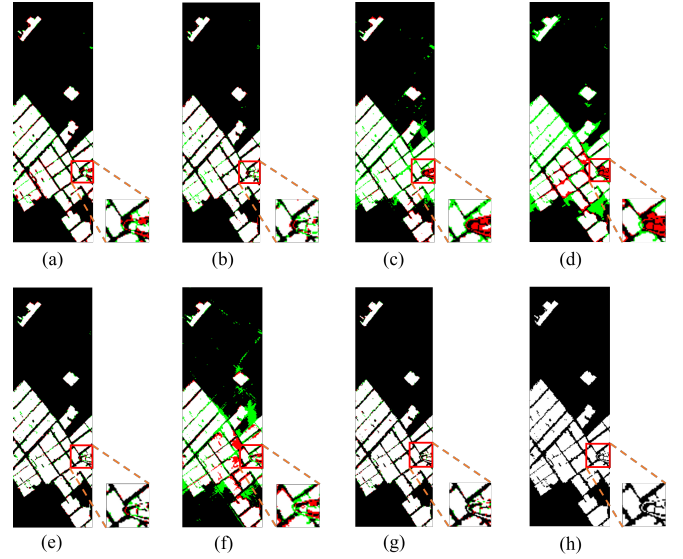


Fig. 13. Visualization results of different detection methods on the Farmland dataset. (a) MHCD, (b) MsFNet, (c) Diefen, (d) AIWSEN, (e) MSDFFN, (f) DA-former, (g) Ours, (h) Change ground truth.

a significant number of green pixels, indicating these methods have limited ability to correctly identify unchanged regions. In contrast, MHCD and MsFNet show fewer green and red pixels, suggesting moderate levels of false positives and false negatives. MSDFFN and CHMFFN further reduce such errors, with their result images exhibiting minimal green and red pixels. To illustrate these differences more clearly, we performed local magnification on the visual results, as shown in Fig. 13(a)-(h). It can be observed that Fig. 13(a) and Fig. 13(b) display noticeably more green and red pixels than Fig. 13(h), while Fig. 13(e) and Fig. 13(g) contain similar amounts. A detailed inspection reveals that the locally magnified results of the six baseline methods (Diefen, AIWSEN, DA-former, MHCD, MsFNet, and MSDFFN) contain more errors than CHMFFN. Overall, the CHMFFN model produces results with the fewest green and red pixels, indicating lower false positive and false negative rates. This demonstrates the superior performance of the proposed method in accurately detecting change regions.

2) *Experimental Results on the Hermiston2 Dataset*: Table II presents the performance of each model on the Hermiston2 dataset. Compared with the MHCD method, other supervised learning methods achieve better performance across all evaluation metrics, particularly in OA and KC. This suggests that MHCD exhibits inferior classification performance and

TABLE II
COMPARISON BETWEEN CHMFFN AND VARIOUS METHODS ON THE HERMISTON2 DATASET

Method	OA (%)	KC (%)	F1 (%)	Pr (%)	Re (%)
MHCD	87.80	62.99	70.62	77.23	65.05
MsFNet	95.30	86.02	88.99	94.30	84.25
DIEFEN	93.91	82.13	86.02	89.16	83.09
AIWSEN	95.26	86.50	89.57	88.78	90.34
MSDFFN	97.66	93.26	94.76	95.74	93.81
DA-former	94.26	83.14	86.80	90.16	83.68
Ours	97.99	94.24	95.54	95.68	95.40

a weak capacity to distinguish between changed and unchanged regions, thereby limiting its overall effectiveness. In contrast, methods such as MsFNet, AIWSEN, MSDFFN, and the proposed CHMFFN consistently yield superior results relative to MHCD, DIEFEN, and DA-Former, due to their enhanced ability to extract discriminative change features and improve change detection accuracy. Notably, MSDFFN and CHMFFN, which incorporate advanced feature learning mechanisms, outperform those relying solely on conventional feature extraction, underscoring the importance of efficient feature representation in adapting to complex change detection scenarios. Moreover, compared with MSDFFN, our CHMFFN achieves further improvements in overall performance by better balancing precision and recall, leading to more accurate and comprehensive identification of changed pixels.

For ease of intuitive observation, the experimental results in Table II are converted into visual representations, as shown in Fig. 14. From the overall visualization, the result images generated by MHCD, MsFNet, and DIEFEN contain a large number of red pixels and relatively few green pixels, indicating a high false negative rate in these methods. In contrast, the visual outputs of AIWSEN and DA-Former display only a small number of red and green pixels, suggesting that both methods achieve relatively low false positive and false negative rates. Meanwhile, MSDFFN and CHMFFN produce result images with very few red and green pixels, indicating more accurate detection performance. To further illustrate these observations, localized zoom-in views of the result images are provided in Figs. 14(a)–(h). From these magnified views, it can be seen that Figs. 14(a), 14(b), 14(c), 14(d), and 14(f) contain noticeably more red and green pixels compared to Figs. 14(e) and 14(g), while the pixel distribution in Fig. 14(e) is visually similar to that in Fig. 14(g). These detailed comparisons reveal that the six methods (DIEFEN, AIWSEN, DA-Former, MHCD, MsFNet, and MSDFFN) generally exhibit more detection errors (false positives and false negatives) than CHMFFN. In summary, the CHMFFN method proposed in this study consistently produces fewer green and red pixels across visual results, reflecting a lower false positive rate and false negative rate. This confirms the superior change detection capability of CHMFFN compared to other baseline methods.

3) *Experimental Results on the Hermiston Dataset:* Table III presents the performance of each model on the Hermiston dataset. Compared to the DIEFEN method, other approaches achieve better results across all evaluation metrics, with particularly significant improvements in Pr and OA. This suggests

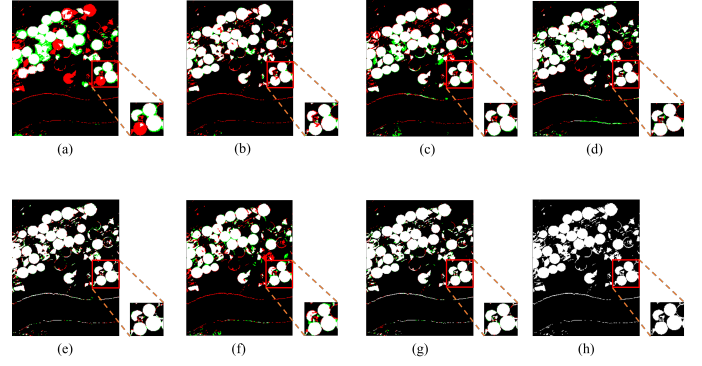


Fig. 14. Visualization results of different detection methods on the Hermiston2 dataset. (a) MHCD, (b) MsFNet, (c) DIEFEN, (d) AIWSEN, (e) MSDFFN, (f) DA-former, (g) Ours, (h) Change ground truth.

TABLE III
COMPARISON BETWEEN CHMFFN AND VARIOUS METHODS ON THE HERMISTON DATASET

Method	OA (%)	KC (%)	F1 (%)	Pr (%)	Re (%)
MHCD	99.17	96.32	96.80	96.06	97.55
MsFNet	99.11	96.00	96.51	97.40	95.63
DIEFEN	98.58	93.83	94.64	91.64	97.86
AIWSEN	98.91	95.12	95.75	95.27	96.22
MSDFFN	99.55	98.01	98.26	97.91	98.61
DA-former	98.73	94.30	95.03	94.92	95.13
Ours	99.64	98.41	98.61	98.71	98.52

that the DIEFEN algorithm tends to produce a higher number of false positives and lacks the ability to accurately delineate changed regions, thereby limiting its overall performance. In contrast, methods such as MHCD, AIWSEN, MSDFFN, and the proposed approach demonstrate consistently superior performance compared to DIEFEN and DA-Former. This improvement can be attributed to their enhanced capability in accurately detecting changed areas, effectively suppressing false positives, and improving overall change detection performance. Among these, MSDFFN and the proposed method exhibit the most remarkable results, benefiting from more efficient feature extraction and processing mechanisms. This underscores the importance of advanced architectures in enabling the network to capture finer-grained change features and handle complex land surface changes. Furthermore, compared to MSDFFN, the proposed method achieves additional gains across all metrics. These improvements stem from its superior feature fusion strategy and more effective classification decisions, leading to more robust and comprehensive detection performance.

For more intuitive observation, the experimental results in Table III are visualized in Fig. 15. Overall, the DIEFEN results exhibit a marginally higher proportion of green pixels compared to other methods, suggesting a relatively higher false positive rate. In contrast, other methods show a relatively balanced distribution of red and green pixels, indicating similar performance levels. To further clarify this observation, we provide localized enlargements of the visual outputs in Fig. 15(a)–(h). From these magnified regions, it is evident that Fig. 15(b) and Fig. 15(f) contain the highest concentration of red

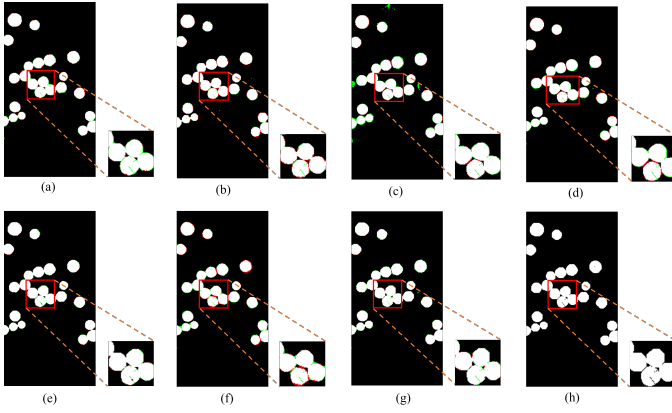


Fig. 15. Visualization results of different detection methods on the Hermiston dataset. (a) MHCD, (b) MsFNet, (c) Diefen, (d) AIWSEN, (e) MSDFFN, (f) DA-former, (g) Ours, (h) Change ground truth.

pixels, while Fig. 15(a) and Fig. 15(c) show a relatively greater presence of green pixels. Additionally, compared to the locally magnified image of CHMFFN, the corresponding regions of the six other methods (DIEFEN, AIWSEN, DA-Former, MHCD, MsFNet, and MSDFFN) contain more red and green pixels, although the differences are not particularly large. In summary, the CHMFFN model produces visual outputs with fewer red and green pixels, implying lower false positive and false negative rates. This suggests that the proposed method achieves superior change detection performance compared to other baseline methods.

4) *Experimental Results on the River Dataset:* Table IV presents the results of various models on the River dataset. Compared with DA-former and MsFNet, the other methods achieve better performance across all evaluation metrics, with particularly notable improvements in OA and KC. This indicates that DA-former and MsFNet do not exhibit significant advantages in classification tasks. Their overall performance is relatively weak, and they demonstrate limited ability in detecting change information. In contrast, MHCD, MSDFFN, and the proposed CHMFFN generally show superior performance compared to DA-former, MsFNet, Diefen, and AIWSEN. These methods are more effective in handling the complex scenarios presented in this dataset, thereby improving both the accuracy and coverage of the classification. Among them, MSDFFN and CHMFFN benefit from stronger feature learning and processing capabilities, leading to better overall results than methods with more moderate performance. This suggests that enhanced feature processing enables the network to capture more discriminative change features, which is crucial for accurate change detection in the River dataset. Furthermore, the proposed CHMFFN achieves further improvements over MSDFFN in all metrics. This is attributed to its ability to better balance precision and recall, resulting in more accurate identification of change information and superior overall performance.

For intuitive observation, the experimental results in Table IV are visualized in Fig. 16. Overall, the number of red and green pixels in Fig. 16(a)–(d) and Fig. 16(f) is significantly higher than in Fig. 16(e) and Fig. 16(g). Notably, these images

TABLE IV
COMPARISON BETWEEN CHMFFN AND VARIOUS METHODS ON THE RIVER DATASET

Method	OA (%)	KC (%)	F1 (%)	Pr (%)	Re (%)
MHCD	96.38	75.34	77.29	85.01	70.86
MsFNet	95.47	69.18	71.62	78.65	65.75
DIEFEN	95.83	70.76	72.98	83.40	64.88
AIWSEN	96.27	75.89	77.92	80.35	75.63
MSDFFN	97.96	86.96	88.07	89.47	86.72
DA-former	95.36	69.56	72.06	76.17	68.73
Ours	98.30	89.26	90.19	90.40	89.99

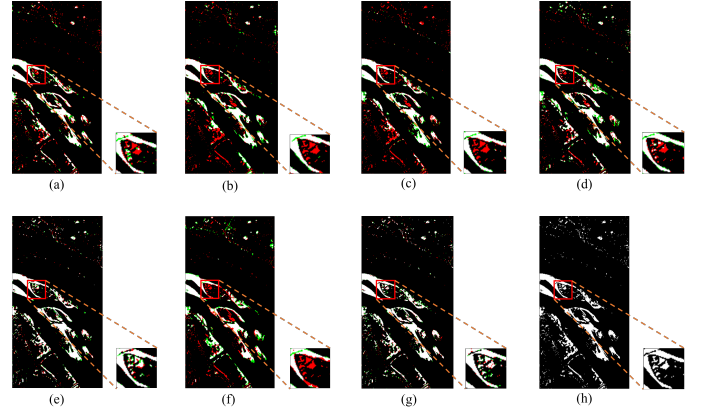


Fig. 16. Visualization results of different detection methods on the River dataset. (a) MHCD, (b) MsFNet, (c) Diefen, (d) AIWSEN, (e) MSDFFN, (f) DA-former, (g) Ours, (h) Change ground truth.

exhibit regions with an excess of red pixels and a scarcity of green pixels, indicating that the MHCD, MsFNet, Diefen, AIWSEN, and DA-Former methods suffer from high false negative and false positive rates. In contrast, the result images of MSDFFN and CHMFFN contain relatively fewer red and green pixels, suggesting lower false detection rates. To further support this observation, local magnification was applied to all visualized results. The zoomed-in views show that the number of green pixels in Fig. 16(e) is slightly greater than in Fig. 16(g), and the red pixel count in the magnified results of the five aforementioned methods is higher than that of CHMFFN. In comparison, the CHMFFN method proposed in this study produces the fewest red and green pixels overall, indicating its superior performance in change detection with reduced false positives and false negatives.

D. Ablation Experiments

To more clearly demonstrate the effectiveness of the designed modules, ablation experiments were conducted on each of the four modules across four datasets, including the Multi-Scale Convolution module (MSC), DCCSA module, STCFL module, and AFAP module. Specifically, four groups of experiments were designed by sequentially removing one module at a time, denoted as A to D.

The experimental results are shown in Table V. Compared with the complete model, the accuracy of the ablated models generally declines, with the complete model achieving the best overall performance. These results provide strong evidence

TABLE V
ABLATION EXPERIMENT RESULTS OF MODULE COMPARISON ON THE
FOUR DATASETS

Dataset	Module	A	B	C	D	Full model
Farmland	MSC	×	✓	✓	✓	✓
	DCCSA	✓	×	✓	✓	✓
	STCFL	✓	✓	×	✓	✓
	AFAF	✓	✓	✓	×	✓
Farmland	OA (%)	98.06	97.55	98.57	97.99	98.61
	KC (%)	95.89	96.62	96.68	95.76	96.77
	F1 (%)	97.01	97.48	97.47	96.02	97.78
	Pr (%)	97.04	97.11	97.28	96.07	97.53
	Re (%)	96.98	97.85	97.66	95.98	98.04
Hermiston2	OA (%)	97.36	97.73	97.68	97.27	97.99
	KC (%)	94.10	93.51	93.24	94.16	94.24
	F1 (%)	94.43	94.97	94.25	94.97	95.54
	Pr (%)	94.85	94.76	95.98	95.13	95.68
	Re (%)	94.01	95.19	92.58	94.81	89.99
Hermiston	OA (%)	98.63	98.65	98.01	98.11	99.64
	KC (%)	97.37	98.12	98.23	98.08	98.41
	F1 (%)	98.08	97.62	98.46	97.67	98.61
	Pr (%)	97.85	97.36	98.36	98.26	98.71
	Re (%)	98.32	97.89	98.56	97.09	98.52
River	OA (%)	98.02	98.01	98.09	98.17	98.30
	KC (%)	87.95	89.13	87.98	89.04	89.26
	F1 (%)	87.15	89.67	89.03	89.54	90.19
	Pr (%)	85.70	89.84	88.69	89.61	90.40
	Re (%)	88.66	89.50	89.37	89.47	89.99

for the effectiveness of each module. Specifically, for the Farmland and River datasets, the OA, KC, F1, Re, and Pr metrics of the complete model all reach optimal values. On the Hermiston dataset, the highest Re and Pr values are observed in the experiment using the module combination “MSC + DCCSA + AFAF”, which surpass those of the complete model. It should be noted that Recall reflects the proportion of correctly identified changed pixels relative to the total number of changed pixels, whereas Precision indicates the proportion of correctly predicted changed pixels among all predicted changes. Due to the imbalance between changed and unchanged pixels, it is possible to observe high Re or Pr values individually, which may result in misleading evaluations if either metric is considered in isolation. As the harmonic mean of Pr and Re, the F1 score balances the two and serves as a more appropriate evaluation metric. Notably, the complete CHMFFN model achieves the highest F1 score across all datasets. Overall, the proposed CHMFFN method effectively identifies changes in ground object states by analyzing the differences between hyperspectral data across different temporal phases. While certain modules may exhibit minor adverse effects on specific datasets, they consistently enhance change detection performance across the majority of experimental scenarios.

E. Discussion

1) Discussion on the setting of training sample proportion:

As a key factor in deep learning model training, the training sample proportion significantly affects both feature learning and generalization of the CHMFFN model. To verify the suitability of setting it to 30%, comparative experiments were

TABLE VI
RESULTS OF DIFFERENT TRAINING SAMPLE PROPORTIONS ON THE FOUR
DATASETS

Dataset	Sample ratio (%)	5	10	20	30
Farmland	OA (%)	97.12	97.67	98.21	98.61
	KC (%)	93.33	94.60	95.86	96.77
	F1 (%)	95.44	96.30	97.16	97.78
	Pr (%)	94.49	95.77	96.72	97.53
	Re (%)	96.40	96.83	97.60	98.04
Hermiston2	OA (%)	95.89	96.74	97.75	97.99
	KC (%)	88.29	90.57	93.49	94.24
	F1 (%)	90.94	92.67	94.94	95.54
	Pr (%)	90.39	93.88	96.06	95.68
	Re (%)	91.50	91.48	93.85	95.40
Hermiston	OA (%)	99.19	99.35	99.52	99.64
	KC (%)	96.39	97.11	97.85	98.41
	F1 (%)	96.86	97.48	97.63	98.61
	Pr (%)	95.91	97.20	97.31	98.71
	Re (%)	97.83	97.77	97.96	98.52
River	OA (%)	96.61	97.40	97.93	98.30
	KC (%)	78.26	83.65	86.85	89.26
	F1 (%)	80.12	85.07	87.98	90.19
	Pr (%)	81.59	84.97	88.99	90.40
	Re (%)	78.70	85.17	87.00	89.99

conducted on four datasets with proportions of 5%, 10%, 20%, and 30%, while keeping all other hyperparameters fixed. The results in Table VI support the comparative analysis and validation of this choice.

The results show that a 30% training sample proportion yields peak OA and KC on the Farmland, Hermiston, and River datasets, confirming its suitability for feature learning. Although the Hermiston2 dataset achieves a local optimum in Pr at 20%, likely due to the higher proportion of unchanged pixels at 30%, the 30% setting offers the most balanced performance overall, mitigating underfitting at small proportions and avoiding overfitting at larger ones.

2) *Discussion on the size of input image patches:* The input image patch size critically affects hyperspectral change detection performance. To assess the impact of spatial context, multi-scale experiments were conducted on four datasets with patch sizes of 5×5, 7×7, and 9×9, while keeping all other hyperparameters fixed. The results are summarized in Table VII for further analysis.

The experimental results show that a 9×9 input patch size consistently achieves the best OA and KC across all datasets. This is attributed to its ability to capture richer neighborhood context, enlarge the receptive field, and enhance spatial-spectral feature fusion, which is crucial for distinguishing subtle changes in complex scenarios. By providing more discriminative contextual information, the 9×9 setting improves feature robustness while maintaining computational efficiency, and is therefore adopted as the final configuration.

3) *Discussion on input batch size:* As a key hyperparameter in deep learning, batch size influences both performance and efficiency in HCD tasks. To determine the optimal setting, this study compared batch sizes of 32, 64, and 128 under identical conditions, with results summarized in Table VIII.

Analysis of the four datasets shows that larger batch sizes lead to a consistent decline in OA and KC. A batch size of 32

TABLE VII
RESULTS OF DIFFERENT INPUT IMAGE PATCH SIZES ON THE FOUR DATASETS

Dataset	Patch size	5×5	7×7	9×9
Farmland	OA (%)	97.19	98.41	98.61
	KC (%)	96.03	96.38	96.77
	F1 (%)	96.51	97.29	97.78
	Pr (%)	96.86	97.20	97.53
	Re (%)	96.16	97.39	98.04
Hermiston2	OA (%)	97.42	97.93	97.99
	KC (%)	93.76	94.08	94.24
	F1 (%)	94.63	95.17	95.54
	Pr (%)	95.01	95.08	95.68
	Re (%)	94.25	95.26	95.40
Hermiston	OA (%)	98.68	99.41	99.64
	KC (%)	98.12	98.24	98.41
	F1 (%)	97.86	98.02	98.61
	Pr (%)	98.02	97.98	98.71
	Re (%)	97.71	98.07	98.52
River	OA (%)	97.28	98.13	98.30
	KC (%)	87.24	88.51	89.26
	F1 (%)	87.18	88.10	90.19
	Pr (%)	86.28	87.02	90.40
	Re (%)	88.10	89.20	89.99

TABLE VIII
RESULTS OF DIFFERENT INPUT BATCH SIZES ON THE FOUR DATASETS

Dataset	Batch size	32	64	128
Farmland	OA (%)	98.61	98.09	97.51
	KC (%)	96.77	96.02	95.52
	F1 (%)	97.78	97.75	97.36
	Pr (%)	97.53	97.47	97.16
	Re (%)	98.04	98.02	97.56
Hermiston2	OA (%)	97.99	97.43	96.82
	KC (%)	94.24	93.49	92.17
	F1 (%)	95.54	95.14	94.20
	Pr (%)	95.68	96.01	94.98
	Re (%)	95.40	94.29	93.44
Hermiston	OA (%)	99.64	98.54	98.02
	KC (%)	98.41	97.38	97.02
	F1 (%)	98.61	98.09	97.13
	Pr (%)	98.71	98.36	98.05
	Re (%)	98.52	97.83	96.23
River	OA (%)	98.30	97.52	96.03
	KC (%)	89.26	88.12	87.02
	F1 (%)	90.19	89.58	88.97
	Pr (%)	90.40	89.79	88.88
	Re (%)	89.99	89.38	89.06

yields optimal results across most metrics, with only slightly lower Pr on the Hermiston dataset due to class imbalance. Overall, smaller batch sizes enhance performance, and thus 32 is adopted as the final setting, balancing efficiency and accuracy in HCD tasks.

IV. CONCLUSION

To address the insufficient exploitation of multiscale features in existing HCD methods, this paper proposes a detection framework referred to as CHMFFN, which incorporates several carefully designed components, including a multiscale encoder-decoder, residual connections, the improved attention mechanism DCCSA, and CNNs. The multiscale feature ex-

traction sub-network is designed to extract and preliminarily fuse features through multiscale convolution blocks and an encoder-decoder structure. Subsequently, the STCFL module is embedded to more effectively learn and represent spectral-spatial-temporal features. Finally, the proposed AFAF module performs the ultimate fusion of high-level features output by the STCFL module, followed by an MLP classifier for pixel-level change detection. Extensive experiments conducted on four publicly available datasets demonstrate that CHMFFN can fully exploit hierarchical representations from multi-temporal HSI and multiscale spectral-spatial-temporal features, thereby significantly enhancing the accuracy of hyperspectral change detection. In future work, we plan to develop a semi-supervised change detection framework that leverages a limited amount of labeled data together with abundant unlabeled data. This approach aims to enhance model generalization by mining latent information from the unlabeled data, which is particularly valuable in scenarios where labeled samples are expensive or difficult to obtain.

REFERENCES

- [1] M. Hu, C. Wu, and L. Zhang, "HyperNet: Self-supervised hyperspectral spatial-spectral feature understanding network for hyperspectral change detection," *IEEE Transactions on Geoscience and Remote Sensing*, vol. 60, pp. 1–17, 2022.
- [2] Y. Wang, D. Hong, J. Sha, L. Gao, L. Liu, Y. Zhang, and X. Rong, "Spectral-spatial-temporal transformers for hyperspectral image change detection," *IEEE Transactions on Geoscience and Remote Sensing*, vol. 60, pp. 1–14, 2022.
- [3] S. Liu, D. Marinelli, L. Bruzzone, and F. Bovolo, "A review of change detection in multitemporal hyperspectral images: Current techniques, applications, and challenges," *IEEE Geoscience and Remote Sensing Magazine*, vol. 7, no. 2, pp. 140–158, 2019.
- [4] Z. Hou, W. Li, L. Li, R. Tao, and Q. Du, "Hyperspectral change detection based on multiple morphological profiles," *IEEE Transactions on Geoscience and Remote Sensing*, vol. 60, pp. 1–12, 2021.
- [5] L. Ding, D. Hong, M. Zhao, H. Chen, C. Li, J. Deng, N. Yokoya, L. Bruzzone, and J. Chanussot, "A survey of sample-efficient deep learning for change detection in remote sensing: Tasks, strategies, and challenges," *IEEE Geoscience and Remote Sensing Magazine*, 2025.
- [6] X. Ou, L. Liu, S. Tan, G. Zhang, W. Li, and B. Tu, "A hyperspectral image change detection framework with self-supervised contrastive learning pretrained model," *IEEE Journal of Selected Topics in Applied Earth Observations and Remote Sensing*, vol. 15, pp. 7724–7740, 2022.
- [7] A. Shafique, S. T. Seydi, T. Alipour-Fard, G. Cao, and D. Yang, "Ssvit-hcd: A spatial-spectral convolutional vision transformer for hyperspectral change detection," *IEEE Journal of Selected Topics in Applied Earth Observations and Remote Sensing*, vol. 16, pp. 6487–6504, 2023.
- [8] Z. Lv, H. Wang, W. Li, and M. Zhang, "Multiscale difference feature-fusion network for change detection with hyperspectral remote sensing images," *IEEE Geoscience and Remote Sensing Letters*, vol. 22, pp. 1–5, 2025.
- [9] H. Zhuang, K. Deng, H. Fan, and M. Yu, "Strategies combining spectral angle mapper and change vector analysis to unsupervised change detection in multispectral images," *IEEE Geoscience and Remote Sensing Letters*, vol. 13, no. 5, pp. 681–685, 2016.
- [10] S. Saha, F. Bovolo, and L. Bruzzone, "Unsupervised deep change vector analysis for multiple-change detection in vhr images," *IEEE transactions on geoscience and remote sensing*, vol. 57, no. 6, pp. 3677–3693, 2019.
- [11] J. Deng, K. Wang, Y. Deng, and G. Qi, "Pca-based land-use change detection and analysis using multitemporal and multisensor satellite data," *International Journal of Remote Sensing*, vol. 29, no. 16, pp. 4823–4838, 2008.
- [12] Z. Lv, T. Liu, C. Shi, J. A. Benediktsson, and H. Du, "Novel land cover change detection method based on k-means clustering and adaptive majority voting using bitemporal remote sensing images," *Ieee Access*, vol. 7, pp. 34425–34437, 2019.
- [13] J. Zhong and R. Wang, "Multi-temporal remote sensing change detection based on independent component analysis," *International Journal of Remote Sensing*, vol. 27, no. 10, pp. 2055–2061, 2006.

- [14] C. Zhou, Q. Shi, D. He, B. Tu, H. Li, and A. Plaza, "Spectral-spatial sequence characteristics-based convolutional transformer for hyperspectral change detection," *CAAI Transactions on Intelligence Technology*, vol. 8, no. 4, pp. 1237–1257, 2023.
- [15] A. Song, J. Choi, Y. Han, and Y. Kim, "Change detection in hyperspectral images using recurrent 3d fully convolutional networks," *Remote Sensing*, vol. 10, no. 11, p. 1827, 2018.
- [16] F. Luo, T. Zhou, J. Liu, T. Guo, X. Gong, and X. Gao, "Dcenet: Diff-feature contrast enhancement network for semi-supervised hyperspectral change detection," *IEEE Transactions on Geoscience and Remote Sensing*, vol. 62, pp. 1–14, 2024.
- [17] F. Jiang, S. Zhang, M. Zhang, M. Gong, Y. Zhou, W. Zhao, and Z. Guan, "Adaptive center-focused hybrid attention network for change detection in hyperspectral images," *IEEE Transactions on Geoscience and Remote Sensing*, vol. 63, pp. 1–16, 2025.
- [18] X. Ou, L. Liu, B. Tu, G. Zhang, and Z. Xu, "A cnn framework with slow-fast band selection and feature fusion grouping for hyperspectral image change detection," *IEEE transactions on geoscience and remote sensing*, vol. 60, pp. 1–16, 2022.
- [19] S. T. Seydi and M. Hasanlou, "A new structure for binary and multiple hyperspectral change detection based on spectral unmixing and convolutional neural network," *Measurement*, vol. 186, p. 110137, 2021.
- [20] Z. Zheng, Y. Wan, Y. Zhang, S. Xiang, D. Peng, and B. Zhang, "Clnet: Cross-layer convolutional neural network for change detection in optical remote sensing imagery," *ISPRS Journal of Photogrammetry and Remote Sensing*, vol. 175, pp. 247–267, 2021.
- [21] X. Zhang, S. Tian, G. Wang, X. Tang, J. Feng, and L. Jiao, "Cast: A cascade spectral-aware transformer for hyperspectral image change detection," *IEEE Transactions on Geoscience and Remote Sensing*, vol. 61, pp. 1–14, 2023.
- [22] Y. Zhang, T. Wang, C. Zhang, S. Xu, H. Gao, and C. Li, "A dual-branch siamese spatial-spectral transformer attention network for hyperspectral image change detection," *Expert Systems with Applications*, vol. 238, p. 122125, 2024.
- [23] Y. Lin, S. Liu, Y. Zheng, X. Tong, H. Xie, H. Zhu, K. Du, H. Zhao, and J. Zhang, "An unsupervised transformer-based multivariate alteration detection approach for change detection in vhr remote sensing images," *IEEE Journal of Selected Topics in Applied Earth Observations and Remote Sensing*, vol. 17, pp. 3251–3261, 2024.
- [24] Y. Li, J. Ren, H. Fu, and G. Sun, "Gassm: Global attention and state space model based end-to-end hyperspectral change detection," *Journal of the Franklin Institute*, vol. 362, no. 3, p. 107424, 2025.
- [25] Y. Ji, W. Sun, Y. Wang, Z. Lv, G. Yang, Y. Zhan, and C. Li, "Domain adaptive and interactive differential attention network for remote sensing image change detection," *IEEE Transactions on Geoscience and Remote Sensing*, vol. 62, pp. 1–16, 2024.
- [26] M. Gong, F. Jiang, A. K. Qin, T. Liu, T. Zhan, D. Lu, H. Zheng, and M. Zhang, "A spectral and spatial attention network for change detection in hyperspectral images," *IEEE Transactions on Geoscience and Remote Sensing*, vol. 60, pp. 1–14, 2021.
- [27] M. Hu, C. Wu, and L. Zhang, "Globalmind: Global multi-head interactive self-attention network for hyperspectral change detection," *ISPRS Journal of Photogrammetry and Remote Sensing*, vol. 211, pp. 465–483, 2024.
- [28] H. Ren, M. Xia, L. Weng, H. Lin, J. Huang, and K. Hu, "Interactive and supervised dual-mode attention network for remote sensing image change detection," *IEEE Transactions on Geoscience and Remote Sensing*, vol. 63, pp. 1–18, 2025.
- [29] Z. Huang, H. Qiu, M. Hou, Z. Yu, S. Wang, X. Li, J. Wang, Y. Yan, and Y. Liu, "Mcecf: A multiscale complementary enhanced context fusion network for remote sensing change detection," *IEEE Transactions on Geoscience and Remote Sensing*, vol. 63, pp. 1–14, 2025.
- [30] J. Qu, S. Hou, W. Dong, Y. Li, and W. Xie, "A multilevel encoder-decoder attention network for change detection in hyperspectral images," *IEEE Transactions on Geoscience and Remote Sensing*, vol. 60, pp. 1–13, 2021.
- [31] O. B. Özdemir and A. Koz, "3d-cnn and autoencoder-based gas detection in hyperspectral images," *IEEE Journal of Selected Topics in Applied Earth Observations and Remote Sensing*, vol. 16, pp. 1474–1482, 2023.
- [32] C. Han, C. Wu, H. Guo, M. Hu, and H. Chen, "Hanet: A hierarchical attention network for change detection with bitemporal very-high-resolution remote sensing images," *IEEE Journal of Selected Topics in Applied Earth Observations and Remote Sensing*, vol. 16, pp. 3867–3878, 2023.
- [33] P. Yuan, Q. Zhao, X. Zhao, X. Wang, X. Long, and Y. Zheng, "A transformer-based siamese network and an open optical dataset for semantic change detection of remote sensing images," *International Journal of Digital Earth*, vol. 15, no. 1, pp. 1506–1525, 2022.
- [34] L. Wang, L. Wang, Q. Wang, and P. M. Atkinson, "Ssa-siamnet: Spectral-spatial-wise attention-based siamese network for hyperspectral image change detection," *IEEE Transactions on Geoscience and Remote Sensing*, vol. 60, pp. 1–18, 2021.
- [35] Y. Shanguan, J. Li, Z. Chen, L. Ren, and Z. Hua, "Multiscale attention fusion graph network for remote sensing building change detection," *IEEE Transactions on Geoscience and Remote Sensing*, vol. 62, pp. 1–18, 2024.
- [36] X. Tang, H. Zhang, L. Mou, F. Liu, X. Zhang, X. X. Zhu, and L. Jiao, "An unsupervised remote sensing change detection method based on multiscale graph convolutional network and metric learning," *IEEE Transactions on Geoscience and Remote Sensing*, vol. 60, pp. 1–15, 2021.
- [37] X. Qin, Y. Zhang, and Y. Dong, "Domain alignment dynamic spectral and spatial feature fusion for hyperspectral change detection," *IEEE Journal of Selected Topics in Applied Earth Observations and Remote Sensing*, vol. 18, pp. 557–568, 2025.
- [38] P. Jian, Y. Ou, and K. Chen, "Hypergraph self-supervised learning-based joint spectral-spatial-temporal feature representation for hyperspectral image change detection," *IEEE Journal of Selected Topics in Applied Earth Observations and Remote Sensing*, vol. 18, pp. 741–756, 2025.
- [39] J. Deng, G. Gong, G. Zhou, M. Yan, and L. Li, "A gated feature fusion network with meta-encoder and self-calibrating cross module for building change detection in remote sensing images," *IEEE Transactions on Geoscience and Remote Sensing*, vol. 62, pp. 1–16, 2024.
- [40] X. Wu, P. Gamba, J. Feng, R. Shang, X. Zhang, and L. Jiao, "A multitask framework for hyperspectral change detection and band reweighting with unbalanced contrastive learning," *IEEE Transactions on Geoscience and Remote Sensing*, vol. 62, pp. 1–13, 2024.
- [41] Y. Feng, W. Ni, L. Song, and X. Wang, "Msfnet: Multi-scale fusion network based on dynamic spectral features for multi-temporal hyperspectral image change detection," *Remote Sensing*, vol. 16, no. 16, p. 3037, 2024.
- [42] L. Wu, L. Ma, J. Peng, B. Yang, W. Sun, J. Wang, and X. Luo, "Diefen: Differential information-enhanced feature exchange network for hyperspectral change detection," *IEEE Transactions on Geoscience and Remote Sensing*, 2024.
- [43] L. Wu, J. Peng, B. Yang, W. Sun, and Z. Ye, "Aiwisen: Adaptive information weighting and synchronized enhancement network for hyperspectral change detection," *IEEE Transactions on Geoscience and Remote Sensing*, 2025.
- [44] F. Luo, T. Zhou, J. Liu, T. Guo, X. Gong, and J. Ren, "Multiscale diff-changed feature fusion network for hyperspectral image change detection," *IEEE Transactions on Geoscience and Remote Sensing*, vol. 61, pp. 1–13, 2023.
- [45] Y. Wang, J. Sha, L. Gao, Y. Zhang, X. Rong, and C. Zhang, "A semi-supervised domain alignment transformer for hyperspectral images change detection," *IEEE Transactions on Geoscience and Remote Sensing*, vol. 61, pp. 1–11, 2023.